Computational Mechanics manuscript No.
(will be inserted by the editor)

Simulating the temporal change of the active response of arteries by finite elements with high-order time-integrators

Rose Rogin Gilbert · Matthias Grafenhorst · Stefan Hartmann · Zohar Yosibash

Received: date / Accepted: date

Abstract A new numerical method to model the active response of arteries is proposed. Vasoconstrictors and vasodilators in the bloodstream diffuse from the lumen into the arterial wall through the intima and cause the smooth muscle cells, mostly in the media, to contract. We combine the diffusion process with the mechanical model in Yosibash and Priel (2012). Finite element computations of the fully coupled field problem using time-adaptive, high-order time-integration methods based on diagonally-implicit Runge-Kutta methods are investigated with respect to their convergence behavior for linear and non-linear loading paths. Since the blood pressure is periodic, highly non-linear external loading path, the step-size estimation has to be adapted to minimize step-size rejections. An example of an artery analysis that illustrates the advantage of the proposed time-adaptive scheme is provided.

Keywords active response · arteries · anisotropy · diffusion equation · finite element method · time-adaptivity

Prof. Dr.-Ing. Stefan Hartmann · Rose Rogin Gilbert · Matthias Grafenhorst
Institute of Applied Mechanics,
Clausthal University of Technology,
Clausthal-Zellerfeld, Germany
E-mail: stefan.hartmann@tu-clausthal.de

Professor Zohar Yosibash
Computational Mechanics and Experimental Biomechanics Labs
School of Mechanical Engineering
The Iby and Aladar Fleischman Faculty of Engineering
Tel-Aviv University
Ramat-Aviv, Israel
E-mail: yosibash@tauex.tau.ac.il

1 Introduction

Active response of arteries is much less investigated compared to the passive response. An arterial wall is composed of three layers: intima, media and adventitia, of which, only the media and adventitia are assumed to be mechanically relevant. The collagen fibers and elastin matrix are responsible for the passive anisotropic behavior whereas smooth muscle cells (SMCs) are responsible for the active behavior of the artery. The media is composed of collagen fibers, SMCs and elastin. The adventitia, however, contains much less SMCs, and may be considered as not contributing to the active response. Thus, the media contributes to both the active and the passive response while the adventitia contributes only to the passive response of the artery. The total response of an artery is the sum of the active and passive responses. There exist many models for describing the passive response of arteries, see (Fung et al, 1979; Delfino et al, 1997; Holzapfel et al, 2000; Zulliger et al, 2004a; Hollander et al, 2011; Nolan et al, 2014). However, only few investigations address the numerical simulation of the active response. This is discussed in the following.

In human bodies, when agitated or excited, sympathetic activation of the adrenal glands causes the adrenal medulla to release norepinephrine (also called noradrenaline) into the bloodstream which guarantees access to a wide variety of tissues, see (Hamill et al, 1996; De La Lande et al, 1974). The norepinephrine (NE) in the bloodstream diffuses from the lumen into the arterial wall through the intima into the media where the SMCs contract, see (Hermsmeyer, 1983). The contraction of the SMCs present in media may be triggered by chemical, neural or mechanical signals and is known as the *active response* of the artery, see (Humphrey, 2002). Chemical stimuli are what causes most of the contractions in SMCs. It is the contraction of the SMCs in the artery that governs the luminal area and the distensibility and consequently regulates the flow of blood in the artery. It has been experimentally proven that the increased concentration of calcium ions within SMCs regulates the contraction, see (Aoki et al, 1994; Grover and Daniels, 2012). In this paper, the diffusion process of NE into the blood vessel thereby causing the muscle cells to contract is modeled by coupling diffusion equation with the mechanical model based on Yosibash and Priel (2012). Following the implementation of the model in the in-house finite element program Tasafem, finite element analyses are carried out for coupled and time-adaptive simulations.

The SMCs are spindle or fusiform shaped with a nucleus at the center. An SMC bundle is generally in the range $2-10\,\mu m$ thick and $20-200\,\mu m$ long. Contractions in SMCs are much slower than other muscle cells and can resist fatigue for much longer than other types of muscles. This is attributed to the lower rate of oxygen and energy consumption. For more detailed information on the biochemistry of SMCs, see (Barany, 1996; Mecham and Schwartz, 1995). In order to contract, SMCs have to increase the amount of calcium ions in the sarcoplasm. The calcium ions bind to calmodulin protein present in the sarcoplasm to make calcium-calmodulin complex which activates an enzyme called myosin light chain kinase which phosphorylates myosin light chains in

the presence of Adenosine Tri-phosphate (ATP). The phosphorylation of these chains present in the myosin heads leads to cross-bridge formation between the myosin heads and the actin filaments, thereby contracting the smooth muscle. This is known as the sliding filament theory, see (Huxley, 1953). For more detailed understanding of the contraction and the relaxation of the SMCs, see (Klabunde, 2005). The constitutive modeling of the passive response of arteries has been widely addressed in previous publications comparing to works on the active response of arteries. Most of the models proposed are based on one-dimensional formulations. A dynamic model based on the sliding filament theory was proposed by Gestrelius and Borgstrom (1986). The model was then compared to the mechanical response of SMCs in a rat portal vein and was found out to be in good accordance with the experiment under isotonic and isometric conditions. Rachev and Hayashi (1999) proposed a mathematical model assuming the artery to be a thick-walled orthotropic tube made of non-linear, incompressible elastic material. They considered that an active circumferential stress is generated in the wall due to the contraction of the SMCs. This was quantified with the help of an additional non-negative active stress in the arterial wall. It was concluded that the active stress generated by the contraction of the SMCs depends on the intensity of stimulation and the stretch ratio. However, the authors were not able to provide a conclusive relation between the chemical concentration and the active stress. Another limitation of the proposed model was the assumption that the length-active tension relationship and the dose-active tension relationship are independent to each other and separately on the stretch. Zulliger et al (2004b) proposed a pseudo-strain energy to describe the active response of the artery. The SMCs were considered as a structural element when compared to previous proposals where the effects of SMCs were included through generation of active stress. A universal model for the elastic, inelastic and active behavior of arteries was proposed by Itskov and Ehret (2009) based on strain-energy function depending on strain invariants associated with fiber directions were used for this model. The coefficients of the linear combinations of the classical structural and the identity tensor work as weighting factors controlling the anisotropic behavior. Active response and softening could be modeled by changing these weighting factors. A mechanochemical micromechanical model was proposed by Murtada et al (2010) based on Hill's three-component model. A strain-energy function along with an evolution equation was used to model the activation of artery. The authors adopted the model proposed by Hai and Murphy (1988) to model the chemical link between Ca^{2+} ion concentration and muscle contraction. This model was further extended by Murtada et al (2012) to include an additional parameter which incorporates the dependence of filament overlap and the sliding filament theory. For the first time, relaxation of artery was also simulated by the authors. The change in intracellular calcium which has an influence on the stress state of an activated artery was analyzed to determine the role of SMC contraction in large elastic arteries, see (Murtada and Holzapfel, 2014). The model proposed by Murtada et al (2012) was implemented into the finite element framework and was verified using isometric contraction and relax-

ation. A new multiscale mathematical model combining the effects of actin and myosin filament overlap and filament lattice spacing, which also has a significant influence on the active stress state, was proposed by Murtada et al (2017). Stålhand et al (2008), for the first time, proposed a strain-energy function that includes the chemical kinetics and the kinematics to model active response of the artery. However, this model was restricted to one dimension and was further extended by Stålhand et al (2011) to three dimensions. A new model to include the membrane excitation process, myosin phosphorylation process, and the contraction mechanics was proposed by Sharifimajd and Stålhand (2014). Schmitz and Böl (2011) proposed a strain-energy function as a sum of a passive strain-energy function, and an active strain-energy function characterizing the calcium driven chemical contraction of SMCs. The model also included the dispersions of the orientations of SMCs and collagen fibers. Böl et al (2012) extended the proposed strain-energy function to describe the calcium phase of the contraction using the cross-bridge model of Hai and Murphy (1988). A micro-structural constitutive model of active response in the case of porcine coronary media was proposed by Chen et al (2013a) to predict the biaxial response. They also determined the dimensions and orientation of SMCs. This data was coupled with a two-dimensional constitutive model to predict circumferential and axial deformation. However, the limitation is that it is a two-dimensional model. The model was based on a biaxial active strain-energy function proposed by Huo et al (2012). Constitutive formulation of active response of porcine renal artery based on in-vitro biaxial (tension-inflation) tests was provided by Zhou et al (2015). The investigation was limited to fully relaxed or contracted SMCs. The authors concluded that the stimulation of SMCs generates both circumferential as well as axial stress. Pandolfi et al (2016) developed a constitutive model where the active response of the fibers is modeled using a strain-energy function which characterizes the mechanical and electrical behavior of the artery. Stålhand et al (2016) discussed the thermodynamics of SMC contraction to understand better the shortening of the muscles and the heat generated. A strain-energy density function based on Rachev and Hayashi (1999) was proposed by Yosibash and Priel (2012) to model the active response of arteries. The superiority of p-FEMs (high-order spatial discretization using integrated Legendre polynomials) over the h-FEMs for solving the coupled passive-active response was demonstrated in that paper. This is done similarly by (Sepahi et al, 2017), however, with a stronger focus on the numerical treatment. In our paper, the model proposed by Yosibash and Priel (2012) is coupled with diffusion equation to represent the activation of the artery.

The coupling of diffusion with mechanical model is widely used in biomechanics. Tumor growth prediction in different parts of the body like kidney, brain etc. was modeled using reaction-diffusion equation by (Menze et al, 2011; Chen et al, 2013b; Wong et al, 2015). The coupling of linear elasticity and a system of reaction-diffusion and ordinary differential equations were modeled for plant cell wall by (Ptashnyk and Seguin, 2016; Piatnitski and Ptashnyk, 2017). Lefèvre and Mangin (2010) coupled the reaction-diffusion to mechanical

model to human brain development. The concept of coupling of diffusion equations with mechanical models has been used in other fields also. The calcium leaching of cementitious materials within the framework of reactive porous media was formulated using chemo-mechanical damage models, see (Kuhl and Meschke, 2003, 2004; Kuhl et al, 2004a,b).

The numerical treatment of coupling diffusion with mechanical model is similar to thermo-mechanically coupled problem. Ellsiepen and Hartmann (2001) applied high-order time-integration finite elements, based on the previous investigations of Wittekindt (1991) and Fritzen (1997). Here, a consistent application of the method of vertical lines is applied to the resulting system of differential-algebraic equations, see (Hartmann and Rothe, 2013). As a first step, the spatial discretization yielding, in dependence of the underlying problem, algebraic equations, ordinary differential equations (ODE), or differential-algebraic equations (DAE). If the systems are ODEs or DAEs, diagonally-implicit Runge-Kutta methods (DIRK) might be chosen for time-integration. This leads to a system of non-linear equations (depending on the problem). These non-linear equations have to be solved using a Newton-like algorithm. In this respect, we refer to (Hartmann, 2005; Hartmann et al, 2009b; Netz and Hartmann, 2015; Rothe et al, 2015b).

DIRK-methods might show order-reduction phenomena if non-linear Dirichlet boundary conditions are applied. This holds for parabolic and hyperbolic-like problems. These problems can be transferred to DAE-systems if the differential part is of such an equation-type, see (Rothe et al, 2015b). Thus, the order analysis for different loading conditions must be investigated. The order obtained from the simulations are compared to theoretical orders. The goal is to obtain at least second order accuracy to apply error estimation for the time-adaptive scheme. In Grafenhorst et al (2017), order analysis was performed for a thermo-viscoplasticity Perzyna/Chaboche-type model with non-linear kinematic hardening. Time-adaptivity was also extensively discussed by the authors. The difference between dynamic and quasi-static computation was also detailed. In our paper, order analysis is performed for linear as well as non-linear loading paths. In the case of non-linear loading paths, it is widely known that the theoretical order cannot be achieved (order reduction phenomenon). This is overcome using an approach of Alonso-Mallo (2002) and Alonso-Mallo and Cano (2004), where the Dirichlet boundary conditions are integrated as well. Based on these investigations, step-size controlled computations are performed for blood pressure cycles. Blood pressure cycles are highly non-linear external loads over the time requiring step-size controlled schemes, see (Hairer et al, 1993; Gustafsson et al, 1988; Gustafsson, 1994).

The structure of the paper is as follows: first, the constitutive model of the active response is discussed. This is followed by the numerical treatment of the coupled problem, where the concentration of the NE is modeled using the diffusion equation so that an inhomogeneous distribution of the activation is described. In the subsequent section, two examples are provided. The first is used to study the convergence behavior for order analysis using linear and non-linear loading. The second example is to show the advantage of time-

adaptive behavior when a complicated loading condition like pressure cycle of blood flowing through blood vessels is used, combined with the activation of the muscle cells.

The notation in use is defined in the following manner: geometrical vectors are symbolized by $\mathbf{a}$, second-order tensors $\mathbf{A}$ by bold-faced Roman letters, and calligraphic letters $\mathcal{A}$ define fourth order tensors. Furthermore, we introduce matrices at global level symbolized by bold-faced italic letters $\boldsymbol{A}$ and matrices on local level using bold-faced Roman letters $\mathbf{A}$.

2 Constitutive Modeling of the Passive and Active Responses of Artery

The stress response of the artery is assumed to be the sum of the active and passive response of the artery

$$\mathbf{T} = \mathbf{T}_{\text{act}} + \mathbf{T}_{\text{pas}} \tag{1}$$

where $\mathbf{T}$ is the Cauchy stress tensor, $\mathbf{T}_{\text{act}}$ is the active stress part, and $\mathbf{T}_{\text{pas}}$ is the passive stress part. In order to model the passive response of the artery, based on the histological findings by Rhodin (2011), the artery is assumed to be hyperelastic and a strain-energy density function is considered, see (Holzapfel et al, 2000; Nolan et al, 2014), for two family of fibers. A viscoelastic response as mentioned, for example, in (Holzapfel et al, 2002) or shown experimentally in (Gilbert et al, 2016), is neglected. The two fiber directions are defined by $\mathbf{a}_0$ and $\mathbf{a}_1$ with $|\mathbf{a}_0| = |\mathbf{a}_1| = 1$ and form normalized tangent vectors at two helices, see Fig. 1. These vectors are defined by $\mathbf{a}_0 = -Y/R\cos\beta\,\mathbf{e}_x +$

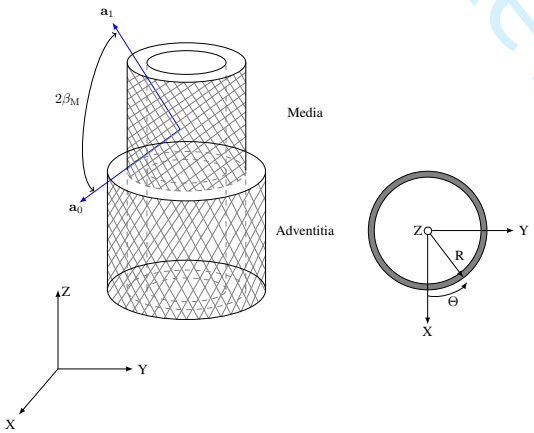

Fig. 1: Helical fibers in an artery

$X/R\cos\beta\,\mathbf{e}_y - \sin\beta\,\mathbf{e}_z$ and $\mathbf{a}_1 = X/R\cos\beta\,\mathbf{e}_x - Y/R\cos\beta\,\mathbf{e}_y + \sin\beta\,\mathbf{e}_z$ in the

case of cylindrical coordinates, where $R = \sqrt{X^2 + Y^2}$. β defines the angle between the circumferential direction and the fiber orientation. The motion of the material body is given by $\mathbf{x} = \boldsymbol{\chi}_R(\mathbf{X}, \mathbf{t})$, where $\mathbf{X}$ represents the material placement vector to point in the reference configuration and $\mathbf{x}$ is the current placement of the point at time t. The deformation gradient, which indicates the local change in deformation, is defined by $\mathbf{F} = \mathrm{Grad}\,\boldsymbol{\chi}_R(\mathbf{X}, t)$. The principal invariants of the right Cauchy-Green tensor $\mathbf{C} = \mathbf{F}^T\mathbf{F}$ are $I_1 = \mathrm{tr}\,\mathbf{C}$, $I_2 = \frac{1}{2}((\mathrm{tr}\,\mathbf{C})^2 - \mathrm{tr}\,\mathbf{C}^2)$ and $I_3 = \det\mathbf{C}$ and the mixed invariants $I_4 = \mathbf{C}\cdot\mathbf{M}_0 = \mathbf{a}_0\cdot\mathbf{C}\mathbf{a}_0$ and $I_6 = \mathbf{C}\cdot\mathbf{M}_1 = \mathbf{a}_1\cdot\mathbf{C}\mathbf{a}_1$ are used to define the strain-energy function

$$\psi_{\mathrm{pas}}(\mathbf{C}, \mathbf{M}_0, \mathbf{M}_1) = \widetilde{\psi}_{\mathrm{pas}}(I_1, I_2, I_3, I_4, I_6). \tag{2}$$

$\mathbf{M}_0 = \mathbf{a}_0\otimes\mathbf{a}_0$ and $\mathbf{M}_1 = \mathbf{a}_1\otimes\mathbf{a}_1$ are called structural tensors. The strain-energy function is decomposed into an isotropic and an anisotropic part

$$\psi_{\mathrm{pas}}(\mathbf{C}, \mathbf{M}_0, \mathbf{M}_1) = \psi_{\mathrm{iso}}(\mathbf{C}) + \psi_{\mathrm{aniso}}(\mathbf{C}, \mathbf{M}_0, \mathbf{M}_1) \tag{3}$$

where the isotropic part is the sum of a volume-changing and a volume-preserving part

$$\psi_{\mathrm{iso}}(J, \overline{\mathbf{C}}) = \psi_{\mathrm{isoch}}(\overline{\mathbf{C}}) + \psi_{\mathrm{vol}}(J). \tag{4}$$

The volume-changing part $\rho_{\mathrm{R}}\psi_{\mathrm{vol}}(J) = K(J^5 + J^{-5} - 2)/50$ depends on the determinant of the deformation gradient $J := \det\mathbf{F}$. With regard to the discussion in (Hartmann and Neff, 2003), the strain-energy function is chosen, instead of the common ansatz $\psi_{\mathrm{vol}}(J) = K/2(J-1)^2$, to circumvent non-physical behavior in tension and compression. The volume-preserving part depends on the unimodular right Cauchy-Green tensor $\overline{\mathbf{C}} = \overline{\mathbf{F}}^T\overline{\mathbf{F}} = (\det\mathbf{C})^{-1/3}\mathbf{C}$ with $\overline{\mathbf{F}} = (\det\mathbf{F})^{-1/3}\mathbf{F}$ and $\det\overline{\mathbf{F}} = 1$. The simplest model is given by the Neo-Hookean model $\rho_{\mathrm{R}}\psi_{\mathrm{isoch}}(I_{\overline{\mathbf{C}}}) = c_{10}(\mathrm{tr}\,\overline{\mathbf{C}} - 3)/2$ with the first invariant $I_{\overline{\mathbf{C}}} = I_1 J^{-2/3}$. Further, following (Nolan et al, 2014), the strain-energy function

$$\psi_{\mathrm{aniso}}(\mathbf{C}, \mathbf{M}_0, \mathbf{M}_1) = \frac{k_1}{2k_2}\left(\left(e^{k_2(I_4-1)^2} - 1\right) + \left(e^{k_2(I_6-1)^2} - 1\right)\right) \tag{5}$$

associated with the fibers is chosen. The second Piola-Kirchhoff tensor for the passive response of the artery reads

$$\begin{aligned}\widetilde{\mathbf{T}}_{\mathrm{pas}} &= 2\rho_{\mathrm{R}}\frac{\partial\psi_{\mathrm{pas}}}{\partial\mathbf{C}} = 2\rho_{\mathrm{R}}\left(\frac{\mathrm{d}\psi_{\mathrm{iso}}}{\mathrm{d}\mathbf{C}} + \frac{\partial\psi_{\mathrm{aniso}}}{\partial\mathbf{C}}\right) = \\ &= \frac{K}{10}(J^5 - J^{-5})\mathbf{C}^{-1} + \\ &+ J^{-2/3}c_{10}\left(\mathbf{I} - \frac{1}{3}(\mathrm{tr}\,\mathbf{C})\mathbf{C}^{-1}\right) + 2k_1\left((I_4 - 1)e^{k_2(I_4-1)^2}\mathbf{M}_0 + (I_6 - 1)e^{k_2(I_6-1)^2}\mathbf{M}_1\right).\end{aligned} \tag{6}$$

Due to the presence of collagen fibers in both the media and the adventitia, the strain-energy function is attributed to both layers (adventitia and media) but having different material parameters in each layer. The active response

of arteries is attributed to the SMCs. The SMCs are assumed to be present only in the media of the artery and thus the active response of the artery is attributed only to the media.

The active response of arteries is based on the concentration of chemicals, where we follow the model presented in Yosibash and Priel (2012). The strain-energy function is based on a proposal of Rachev and Hayashi (1999). Rachev and Hayashi (1999) stated that the concentration A of the vasoconstrictor is proportional to the first Piola-Kirchhoff stress component due to the contraction of the SMCs in the media. The SMCs are also arranged circumferentially in the shape of a helix in the media and are represented by the unit vector $\mathbf{a}_{\mathrm{f}}$. If a ring test is assumed, then the loading is in circumferential direction. In this case, only one component of the first Piola-Kirchhoff tensor is assumed to be addressed. This first Piola-Kirchhoff stress component due to the contraction of SMCs is assumed to read

$$p_{\mathrm{act}} = S(A) f(\lambda_{\mathrm{f}}), \tag{7}$$

where $S(A)$ is the tension-dose relationship and $f(\lambda_{\mathrm{f}})$ is the tension-stretch relationship. The tension-dose relationship follows Chamiot-Clerc et al (1998) and is obtained from a ring test,

$$S(A) = S_{\max} \frac{A^m}{A^m + A_{50}^m}. \tag{8}$$

Here, m is the slope parameter, $S_{\max}$ represents – in this sense – the maximum value of the first Piola-Kirchhoff stress component due to the influence of vasoconstrictor and A_{50} is the concentration at which 50% of maximum tension is achieved and is called the half maximal effective concentration. It was experimentally determined, see (Cox, 1978b), that the contraction in arteries only occur within a certain range of concentration of the neurotransmitter, i.e. the contraction occurs within a minimum and maximum concentration of the vasoconstrictor.

The tension-stretch relation is based on the proposal of Rachev and Hayashi (1999),

$$f(\lambda_{\mathrm{f}}) = \begin{cases} 1 - \left(\frac{\lambda_{\max} - \lambda_{\mathrm{f}}}{\lambda_{\max} - \lambda_0} \right)^2, & \lambda_1 > \lambda_{\mathrm{f}} > \lambda_0 \\ 0 & \text{otherwise,} \end{cases} \tag{9}$$

where $\lambda_{\max}$ is the stretch at which maximum contraction of the artery is possible, and λ_0 and $\lambda_1 = \lambda_0 + 2(\lambda_{\max} - \lambda_0)$ are the minimum and maximum stretches at which the artery contracts. The tension-stretch relationship is obtained from inflation experiments of contraction of SMC under the influence of vasoconstrictor. This relationship has been experimentally proven to be a parabolic curve, see (Cox, 1978a,b; Rachev and Hayashi, 1999). The stretch of the SMC fiber can be represented by the invariant $I_{4\mathrm{f}} = \lambda_{\mathrm{f}}^2 = \mathbf{C} \cdot \mathbf{M}_{\mathrm{f}} = \mathbf{a}_{\mathrm{f}} \cdot \mathbf{C}\mathbf{a}_{\mathrm{f}}$,

where $\mathbf{a}_\mathrm{f}$ is the SMC-direction, and $\mathbf{M}_\mathrm{f} = \mathbf{a}_\mathrm{f} \otimes \mathbf{a}_\mathrm{f}$ the corresponding structural tensor. Eqs.(8) and (9) are substituted in Eq.(7) to obtain

$$p_\mathrm{act} = \begin{cases} S_\mathrm{max} \frac{A^m}{A^m + A_{50}^m} \left[1 - \left(\frac{\lambda_\mathrm{max} - \lambda_\mathrm{f}}{\lambda_\mathrm{max} - \lambda_0} \right)^2 \right], & \lambda_1 > \lambda_\mathrm{f} > \lambda_0 \\ 0 & \text{otherwise.} \end{cases} \tag{10}$$

It is assumed that an active strain-energy function exists. This first Piola-Kirchhoff stress can be obtained by differentiating the active strain-energy function with respect to the muscle stretch, i.e.

$$p_\mathrm{act} = \frac{\partial \psi_\mathrm{act}}{\partial \lambda_\mathrm{f}}. \tag{11}$$

Inserting Eq.(10) into Eq.(11) and then integrating, the expression for ψ_act

$$\psi_\mathrm{act} = \begin{cases} S_\mathrm{max} \frac{A^m}{A^m + A_{50}^m} \left[\frac{(\lambda_\mathrm{max} - \lambda_\mathrm{f})^3}{3(\lambda_\mathrm{max} - \lambda_0)^2} + \lambda_\mathrm{f} \right], & \lambda_1^2 > \lambda_\mathrm{f}^2 > \lambda_0^2 \\ 0 & \text{otherwise,} \end{cases} \tag{12}$$

is obtained. The transition to a three-dimensional model is achieved using the second Piola-Kirchhoff tensor for the active response of the artery is

$$\widetilde{\mathbf{T}}_\mathrm{act} = 2 \frac{\partial \psi_\mathrm{act}}{\partial \mathbf{C}} = S_\mathrm{max} \frac{A^m}{A^m + A_{50}^m} I_\mathrm{4f}^{-1/2} \left(1 - \left(\frac{\lambda_\mathrm{max} - I_\mathrm{4f}^{1/2}}{\lambda_\mathrm{max} - \lambda_0} \right)^2 \right) \mathbf{M}_\mathrm{f}. \tag{13}$$

Pushing forward Eq.(13) and Eq.(6) and substituting the resulting terms in Eq.(1), we obtain the total Cauchy stress tensor for the media,

$$\begin{aligned} \mathbf{T}_\mathrm{M} =& \frac{K_\mathrm{M}}{10} (J^4 - J^{-6}) \mathbf{I} + c_\mathrm{M} J^{-2/3} \overline{\mathbf{B}}^D \\ &+ 2 J^{-1} k_\mathrm{1M} \left((I_4 - 1) e^{k_\mathrm{2M} (I_4 - 1)^2} \mathbf{M}_\mathrm{M0} + (I_6 - 1) e^{k_\mathrm{2M} (I_6 - 1)^2} \mathbf{M}_\mathrm{M1} \right) \\ &+ J^{-1} S_\mathrm{max} \frac{A^m}{A^m + A_{50}^m} I_\mathrm{4f}^{-1/2} \left(1 - \left(\frac{\lambda_\mathrm{max} - I_\mathrm{4f}^{1/2}}{\lambda_\mathrm{max} - \lambda_0} \right)^2 \right) \mathbf{M}_\mathrm{f}. \end{aligned} \tag{14}$$

The total Cauchy stress for the adventitia contains only the passive response $\mathbf{T}_\mathrm{pas}$,

$$\begin{aligned} \mathbf{T}_\mathrm{A} =& \frac{K_\mathrm{A}}{10} (J^4 - J^{-6}) \mathbf{I} + c_\mathrm{A} J^{-2/3} \overline{\mathbf{B}}^D \\ &+ 2 J^{-1} k_\mathrm{1A} \left((I_4 - 1) e^{k_\mathrm{2A} (I_4 - 1)^2} \mathbf{M}_\mathrm{A0} + (I_6 - 1) e^{k_\mathrm{2A} (I_6 - 1)^2} \mathbf{M}_\mathrm{A1} \right). \end{aligned} \tag{15}$$

3 Numerical Treatment using Finite Elements

Frequently, the concentration A in Eqns.(14) is assumed to be only a parameter, which cannot describe the spatial and temporal evolution within a boundary-value problem. In the following, we propose the concentration A as primary variable, which is a result of the diffusion process into the artery. Since the chemicals diffuse into the tissue, see (Hamill et al, 1996), we draw on the diffusion equation to model the temporal and spatial distribution of the concentration A. To couple the diffusion equation with the mechanical model (balance of linear momentum and the constitutive equations), we provide only the basic, resulting equations using finite elements. In this respect, the method of vertical lines is applied, where in a first step the spatial discretization is carried out, here, using finite elements, and, in a second step, the time discretization is applied. Since the resulting equations are similar to those of thermo-mechanically coupled problems, we only shortly recap the equations and refer to the literature.

The local equilibrium condition is based on balance of linear momentum,

$$\operatorname{Div} \mathbf{T}_R(\mathbf{X}, t) + \rho_R(\mathbf{X})\mathbf{k}(\mathbf{X}) = \mathbf{0} \tag{16}$$

where $\mathbf{T}_{\mathrm{R}} = (\det \mathbf{F})\mathbf{F}\mathbf{F}^{-T}$ defines the first Piola-Kirchhoff stress tensor, ρ_{R} represents the specific mass density in reference configuration, and $\rho_{\mathrm{R}}\mathbf{k}$ the specific body forces. To obtain the weak formulation, we multiply Eq.(16) with the virtual displacements $\delta\mathbf{u}(\mathbf{X})$, integrate over the volume, apply the divergence theorem and a product rule, to obtain

$$\int_{V_{\mathrm{R}}} \widetilde{\mathbf{T}} \cdot \delta\mathbf{E} \, \mathrm{d}V_{\mathrm{R}} = \int_{A_{\mathrm{R}}} \mathbf{t}_{\mathrm{R}} \cdot \delta\mathbf{u} \, \mathrm{d}A_{\mathrm{R}} + \int_{V_{\mathrm{R}}} \rho_{\mathrm{R}}\mathbf{k} \cdot \delta\mathbf{u} \, \mathrm{d}V_{\mathrm{R}} \tag{17}$$

where $\widetilde{\mathbf{T}}$ is the second Piola-Kirchhoff tensor, $\widetilde{\mathbf{T}} = (\det \mathbf{F})\mathbf{F}^{-1}\mathbf{T}\mathbf{F}^{-T}$, $\mathbf{t}_{\mathrm{R}}$ the surface tractions relative to the reference configuration, V_{R} the volume and A_{R} the surface in the reference configuration, and $\delta\mathbf{E} = sym(\mathbf{F}^T \delta \operatorname{Grad} \mathbf{u})$ the virtual Green strain tensor.

The governing equation for diffusion process is given by

$$\dot{A} = -\operatorname{div} \mathbf{J} \tag{18}$$

where A is the concentration of NE at the material point $\mathbf{X}$. $\mathbf{J}$ is called the diffusive flux given by Fick's first model (law) relative to the current configuration,

$$\mathbf{J} = -D \operatorname{grad} A, \tag{19}$$

where D is the diffusivity (or diffusion coefficient), which is assumed to be constant. This leads to the partial differential equation

$$\dot{A} = D \operatorname{div}(\operatorname{grad} A). \tag{20}$$

The weak formulation is obtained by multiplying Eq.(20) with the virtual concentration δA, integrating over the volume, drawing on a product rule, and applying the divergence theorem,

$$\int_V \dot{A}\ \delta A \,\mathrm{d}V + \int_V D\,\mathrm{grad}\,A \cdot \mathrm{grad}\,\delta A \,\mathrm{d}V = \int_{\overline{A}} q_\mathrm{A} \delta A \,\mathrm{d}\overline{A}. \tag{21}$$

This is the weak form of the diffusion equation relative to the current configuration. V is the volume of the material body in the current configuration and $\overline{A}$ its surface. q_A represents the surface flux. It is assumed that no neurotransmitter is produced in the media, and, thus, no source term is identified.

To keep the presentation as short as possible, we refer to the spatial discretization in thermo-mechanics, see (Quint, 2012; Rothe, 2015; Netz, 2013; Netz and Hartmann, 2015) and the literature cited therein. In other words, shape functions for virtual concentrations δA and concentrations A are introduced and inserted into Eq.(21). This leads to the DAE-system

$$\boldsymbol{g}(t, \boldsymbol{u}, \boldsymbol{a}) = \boldsymbol{0} \tag{22}$$

$$\boldsymbol{C}(t, \boldsymbol{u})\dot{\boldsymbol{a}} = \boldsymbol{r}_\mathrm{A}(t, \boldsymbol{u}, \boldsymbol{a}), \tag{23}$$

with the unknown nodal displacements $\boldsymbol{u} \in \mathbb{R}^{n_\mathrm{u}}$ and the unknown nodal concentrations $\boldsymbol{a} \in \mathbb{R}^{n_\mathrm{a}}$. $\boldsymbol{C} \in \mathbb{R}^{n_\mathrm{a} \times n_\mathrm{a}}$ represents a mass matrix like matrix. The representation of the matrices is compiled in the Appendix A. The DAE-system is equipped with initial conditions $\boldsymbol{u}(0) = \boldsymbol{u}_0$ and $\boldsymbol{a}(0) = \boldsymbol{a}_0$. The initial conditions have to be consistent, i.e. we have to fulfill the algebraic constraint $\boldsymbol{g}(0, \boldsymbol{u}_0, \boldsymbol{a}_0) = \boldsymbol{0}$. In our examples in Section 4, this is guaranteed by $\boldsymbol{u}_0 = \boldsymbol{0}$, $\boldsymbol{a}_0 = \boldsymbol{0}$, and no external equivalent nodal forces at time $t = 0$. In conclusion, the spatial discretization yields a DAE-system, which requires an appropriate time discretization.

There are different approaches to solve such kind of problems. Apart from discontinuous/continuous Galerkin methods, see, for example, (Gleim et al, 2015), BDF-methods are another choice, (Ascher and Petzold, 1998; Eckert et al, 2004), or fully-implicit Runge-Kutta methods, (Hairer and Wanner, 1996), Rosenbrock-type methods (linear-implicit schemes), (Hamkar and Hartmann, 2012; Hamkar et al, 2012; Hamkar, 2013), half-explicit Runge-Kutta methods, (Hairer et al, 1989; Hairer and Wanner, 1996; Strehmel and Weiner, 1995), or diagonally-implicit Runge-Kutta methods (DIRK), (Fritzen, 1997; Ellsiepen, 1999; Hairer and Wanner, 1996; Netz et al, 2013) can be applied. A comparison of the methods in the finite element context is provided in (Rothe et al, 2012). Regarding partitioned and monolithic approaches, see (Erbts and Düster, 2012; Erbts et al, 2015; Rothe et al, 2015a; Wendt et al, 2015).

For the second step of the method of vertical lines, namely the time discretization, we draw on diagonally-implicit Runge-Kutta methods (DIRK). They have, apart from particular properties for stiff problems, the advantage to contain the classical Backward-Euler method, or even the Crank-Nicolson scheme as special cases. Moreover, high-order convergence and time-adaptivity are provided. Further advantages are, for example, that they are self-starting

(which is a drawback of BDF-schemes) and that the size of the resulting system of coupled non-linear equations remain the same as for the DAE-system itself. Disadvantages such as order reduction phenomena in particular problems are discussed in Section 4. There are various methods: a fourth-order method with an embedded method of third order for step-size selection proposed by (Hairer and Wanner, 1996). A third-order method of Alexander (1977), which was extended by Cash (1979) for time-adaptivity, and a second-order scheme of Alexander (1977) extended to adaptivity in Ellsiepen (1999), see (Diebels et al, 1999; Ellsiepen and Hartmann, 2001) as well.

Since DIRK-methods are one-step methods, the quantities – nodal displacements $\boldsymbol{u}_n$ and nodal concentrations $\boldsymbol{a}_n$ – at time t_n are known. We formally assemble these quantities into the vector $\boldsymbol{y}_n^T = \{\boldsymbol{u}_n^T, \boldsymbol{a}_n^T\}$. The quantities at time t_{n+1} are computed by

$$\boldsymbol{y}_{n+1} = \boldsymbol{y}_n + \Delta t_n \sum_{i=1}^{s} b_i \dot{\boldsymbol{Y}}_{ni} \tag{24}$$

b_i, $i = 1, \ldots, s$, are weighting factors defined by the integration method, $\Delta t_n = t_{n+1} - t_n$ is the step-size, and $\dot{\boldsymbol{Y}}_{ni}$ are stage derivatives, which are stored at each stage $T_{ni} = t_n + c_i \Delta t_n$ (the c_i's are parameters of the respective DIRK-method as well),

$$\dot{\boldsymbol{Y}}_{ni} = \frac{\boldsymbol{Y}_{ni} - \boldsymbol{S}_{ni}}{\Delta t_n a_{ii}}. \tag{25}$$

The starting values

$$\boldsymbol{S}_{ni} = \boldsymbol{y}_n + \Delta t_n \sum_{j=1}^{i-1} a_{ij} \dot{\boldsymbol{Y}}_{ni} \tag{26}$$

are known at each stage T_{ni} since they depend only on quantities computed in the previous stages. The weighting factors a_{ij} are determined for specific DIRK-methods. All factors a_{ij}, c_i and b_i are assembled in the so-called Butcher-array. At each stage T_{ni} a system of coupled non-linear equations

$$\begin{aligned} \boldsymbol{G}_{\mathrm{u}}(T_{ni}, \boldsymbol{U}_{ni}, \boldsymbol{A}_{ni}) &= \boldsymbol{0} \\ \boldsymbol{G}_{\mathrm{A}}(T_{ni}, \boldsymbol{U}_{ni}, \boldsymbol{A}_{ni}) &= \boldsymbol{0} \end{aligned} \tag{27}$$

has to be solved to obtain the stage quantities $\boldsymbol{Y}_{ni}^T = \{\boldsymbol{U}_{ni}^T, \boldsymbol{A}_{ni}^T\}$. Here,

$$\boldsymbol{G}_{\mathrm{A}}(T_{ni}, \boldsymbol{U}_{ni}, \boldsymbol{A}_{ni}) = \boldsymbol{C}_{\mathrm{A}}(T_{ni}, \boldsymbol{u}_{ni})\{\boldsymbol{A}_{ni} - \boldsymbol{A}_{ni}^S\} - \Delta t_n a_{ii} \boldsymbol{r}_{ni}\left(T_{ni}, \boldsymbol{U}_{ni}, \frac{\boldsymbol{U}_{ni} - \boldsymbol{U}_{ni}^S}{\Delta t_n a_{ii}}, \boldsymbol{A}_{ni}\right), \tag{28}$$

where different techniques are available, (Hartmann et al, 2009a). $\boldsymbol{U}_{ni}^S$ and $\boldsymbol{A}_{ni}^S$ are the starting values depending only on stage derivatives already calculated in previous stages, see Eq.(26), $\boldsymbol{S}_{ni}^T = \left\{\boldsymbol{U}_{ni}^{S\,T}\, \boldsymbol{A}_{ni}^{S\,T}\right\}$. Regarding time-adaptivity, i.e. an automatic step-size selection based on local error estimation, see (Hairer et al, 1993; Ellsiepen and Hartmann, 2001) and for coupled problems in (Grafenhorst et al, 2017). Here, we draw on a method of order $\hat{p} = p - 1$

– having new weighting factors $\hat{b}_i$, $i = 1, \ldots, s$ – and compute the difference vectors

$$\begin{aligned} \boldsymbol{u}_{\text{err}} &= \hat{\boldsymbol{u}}_{n+1} - \boldsymbol{u}_{n+1} = \Delta t_n \sum_{i=1}^{s} (\hat{b}_i - b_i) \dot{\boldsymbol{U}}_{ni}, \\ \boldsymbol{a}_{\text{err}} &= \hat{\boldsymbol{a}}_{n+1} - \boldsymbol{a}_{n+1} = \Delta t_n \sum_{i=1}^{s} (\hat{b}_i - b_i) \dot{\boldsymbol{A}}_{ni}. \end{aligned} \tag{29}$$

The components are required for the relative error measures

$$e_{\text{u}} := \sqrt{\frac{1}{n_{\text{u}}} \sum_{k=1}^{n_{\text{u}}} \left(\frac{u_{\text{err}\,k}}{\varepsilon_{\text{r}}^{u} |u_{k(n)}| + \varepsilon_{\text{a}}^{u}} \right)^2}, \qquad e_{\text{A}} := \sqrt{\frac{1}{n_{\text{a}}} \sum_{k=1}^{n_{\text{a}}} \left(\frac{a_{\text{err}\,k}}{\varepsilon_{\text{r}}^{a} |a_{k(n)}| + \varepsilon_{\text{a}}^{a}} \right)^2}, \tag{30}$$

where the maximum $e_{\text{m}} = \max(e_{\text{u}}, e_{\text{A}})$ is chosen to estimate the new step-size. n_{u} and n_{a} are the number of unknown nodal displacements and concentrations respectively. $\varepsilon_{\text{r}}^{u}, \varepsilon_{\text{r}}^{a}$ are relative and $\varepsilon_{\text{a}}^{u}, \varepsilon_{\text{a}}^{a}$ absolute error tolerances for the displacements and concentration degrees of freedom defined by the user. If $e_{\text{m}} \leq 1$, the computed step-size is accepted and we can continue the computations with a new step-size Δt_{new}, otherwise the computations are rejected and we have to repeat it with a new step-size,

$$\Delta t_{\text{new}} = \Delta t_n \times \begin{cases} \max(f_{\min}, f_{\text{safety}}\, \mathrm{e}_m^{-1/(\hat{p}+1)}) & \text{if } \mathrm{e}_m > 1 \\ \min(f_{\max}, f_{\text{safety}}\, \mathrm{e}_m^{-1/(\hat{p}+1)}) & \text{if } \mathrm{e}_m \leq 1 \end{cases} \tag{31}$$

The safety factor $0 < f_{\text{safety}} < 1$ prevents oscillations in the step-size controller while $f_{\min}$ and $f_{\max}$ keep the step-size from increasing and decreasing too fast. In practice, typical values for these factors are: $0.8 \leq f_{\text{safety}} \leq 0.9$, $0.2 \leq f_{\min} \leq 0.5$, $2 \leq f_{\max} \leq 3$, see (Hairer et al, 1993; Ellsiepen and Hartmann, 2001).

This step-size selection procedure works well for physical problems, showing no drastic change in the quantities. In that case, more step-size rejections occur. If this is embedded in periodic processes, too many step-size rejections make the computations not as efficient as they could be. Thus, a modification for cyclic and periodic situations is proposed. The principal idea is to take the history of the step-size selection of the last periods into account.

First, we have to define the starting time t_{start}, when the periodic process leads to more or less periodic step-size selections. Moreover, the period T has to be known, which is defined by the input (mechanical loading) process. Only in the case, when the step-size should be increased the history information is taken into consideration. Here, we can take only one, several, or all cycles into consideration, i.e. the accepted step-sizes are stored at each time t_n for a certain number of cycles. We define the maximum cycles to be considered $n_{\max}$. Then, we look for the step-sizes at the times $t_{\text{old}} = t_n - kT$, $k = 1, \ldots, n_{\max}$, which are in the intervals $t_{1k} \leq t_{\text{old}} \leq t_{2k}$. We take the smaller of the step-sizes concerned, $\Delta t_k = \min(\Delta t_{1k}, \Delta t_{2k})$, and from all chosen step-sizes the largest is chosen, $\Delta t_{\text{old}} = \max_{k=1,\ldots,n_{\max}} \Delta t_k$. This, is used for defining

$$f_{\text{hist}} = f_{\text{old}} \frac{\Delta t_{\text{old}}}{\Delta t_n},$$

where f_{old} has to be adapted to the situation. Later on, we choose $f_{\text{old}} = 1$. The new step-size is estimated by

$$\Delta t_{\text{new}} = \Delta t_n \times \begin{cases} \max(f_{\min}, f_{\text{safety}}\ \mathrm{e}_m^{-1/(\hat{p}+1)}) & \text{if } \mathrm{e}_m > 1 \\ \min(f_{\max}, f_{\text{safety}}\ \mathrm{e}_m^{-1/(\hat{p}+1)}, f_{\text{hist}}) & \text{if } \mathrm{e}_m \leq 1 \end{cases} \tag{32}$$

In other words, there is not only the influence of the current local error estimation, but also the history for cyclic process.

4 Numerical Examples

In the following, we discuss two examples. First, we investigate the order behavior of various DIRK-methods, which are applied to the DAE-system (22) and (23). We will see that order reduction phenomena might occur depending on the Dirichlet boundary conditions. According to (Rothe et al, 2015b) a proposal of (Alonso-Mallo, 2002; Alonso-Mallo and Cano, 2004) is chosen. In the second example, time-adaptive computations are performed on a reconstructed artery, where the internal pressure cycles are overlapped with a spontaneous increase of the noradrenaline concentration at the inner surface. Here, apart from the influence of the diffusivity generating the active response of the artery, the new concept of the step-size selection for periodic processes is considered.

4.1 Order Investigation

We are interested in the order behavior of the DAE-system (22) and (23). The order analysis is performed by taking an example of a quarter of a cylinder which is fixed along the z-axis so as to resemble an artery (symmetry conditions are assumed for displacements), see Fig. 2. For the spatial discretization, twenty-noded hexahedral Lagrange elements are used to obtain $n_{\text{el}} = 1750$ summing up to a total number of $n_{\text{nodes}} = 12728$ nodes. The cylinder is divided into two layers, media and adventitia. The media is assumed to be 4 mm, whereas the adventitia is assumed to has a thickness of 2 mm. The SMCs are assumed to be in circumferential direction. The NE is applied on the inner side of the cylinder as shown in Fig. 2. Initially, the concentration of NE in the entire cylinder is assumed to be $A(\mathbf{X}, 0) = 0$, i.e. the artery is not activated.

4.1.1 Linear Loading Path

As a first step, the cylinder is loaded by a linear increasing concentration varying from 0 to 0.1 nM within one second, see Fig. 3(a). The NE diffuses into the media as well as the adventitia. However, due to the lack of SMCs in the adventitia, it does not actively contract in this region. The contraction of the artery takes place only in the media. This is enforced in the model as described in Section 2. The value of the material parameters are taken from

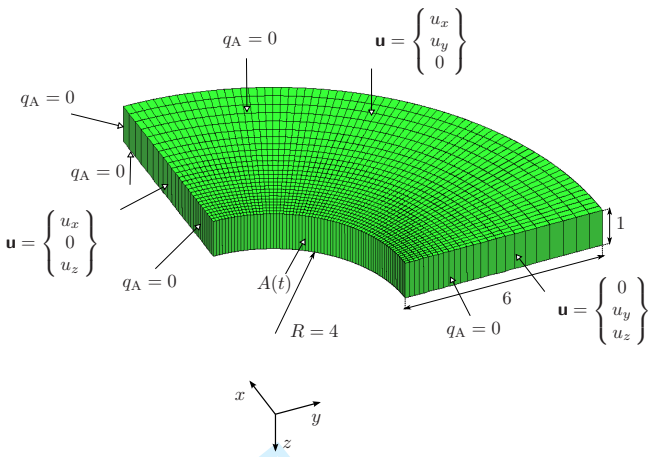

Fig. 2: Geometry, mesh and boundary conditions (units in mm)

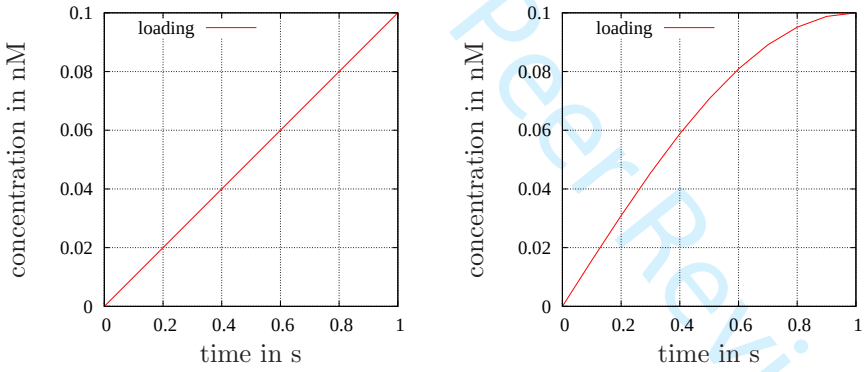

(a) Linear loading path

(b) Non-linear loading path

Fig. 3: Loading paths

Yosibash and Priel (2012) except for the diffusivity of NE in the artery. The diffusivity or diffusion coefficient is assumed in this particular case. The entire material parameter list is compiled in Tab. 1. In the following order study, DIRK-methods of different order (be: Backward-Euler method ($p = 1$, $s = 1$), alex2: second order method of Alexander (1977) ($p = 2$, $s = 2$), alex3: third order method of Alexander (1977) ($p = 3$, $s = 3$), hairer4: fourth order method according to (Hairer and Wanner, 1996) ($p = 4$, $s = 5$)) are used. The factors of the DIRK methods are assembled into a so-called Butcher-Tableau and can be found in Appendix B. The relative error quantities are defined by the

Table 1: Active and passive material parameters (Yosibash and Priel, 2012)

material parameters	**symbol**	**value**	**unit**
bulk modulus - media	K_{M}	6.6667×10^{-1}	$\mathrm{N/mm^2}$
shear modulus - media	G_{M}	2.0×10^{-2}	$\mathrm{N/mm^2}$
angle of helix in media	β_{M}	20	$^\circ$
anisotropic material parameter - media	$k_{1\mathrm{M}}$	6.0×10^{-4}	$\mathrm{N/mm^2}$
anisotropic material parameter - media	$k_{2\mathrm{M}}$	1.2	-
bulk modulus - adventitia	K_{A}	6.6667×10^{-1}	$\mathrm{N/mm^2}$
shear modulus - adventitia	G_{A}	1.0×10^{-2}	$\mathrm{N/mm^2}$
angle of helix in adventitia	β_{A}	64	$^\circ$
anisotropic material parameter - adventitia	$k_{1\mathrm{A}}$	4.0×10^{-4}	$\mathrm{N/mm^2}$
anisotropic material parameter - adventitia	$k_{2\mathrm{A}}$	1.2	-
max. stretch at which contraction of the artery is possible	$\lambda_{\max}$	1.49	-
minimum stretch at which the artery contracts	λ_0	0.85	-
max. value of the 1st PK stress component due to the activation	$S_{\max}$	4.5×10^{-2}	$\mathrm{N/mm^2}$
slope parameter	m	5.9	-
half maximal effective concentration	A_{50}	0.1	nM
diffusivity- media (assumption)	D_{M}	2	$\mathrm{mm^2/s}$
diffusivity- adventitia (assumption)	D_{A}	5	$\mathrm{mm^2/s}$

maximum relative error over all the points in time t_n,

$$\mathrm{err}_{\boldsymbol{u}} = \max_n \left(\frac{\|\boldsymbol{u}_n^{\mathrm{ref}} - \boldsymbol{u}_n\|}{\max_n \left(\|\boldsymbol{u}_n^{\mathrm{ref}}\|\right)} \right), \qquad \mathrm{err}_{\boldsymbol{A}} = \max_n \left(\frac{\|\boldsymbol{A}_n^{\mathrm{ref}} - \boldsymbol{A}_n\|}{\max_n \left(\|\boldsymbol{A}_n^{\mathrm{ref}}\|\right)} \right). \tag{33}$$

In the case of order considerations for the displacement degrees of freedom, except for the Hairer and Wanner method, the other three methods achieve their respective orders, see Fig. 4(a). For the case of the concentration behavior, see Fig. 4(b), all expected orders are reached. The reason of not achieving fourth-order is not known to the authors. Similar results can be found in (Rothe et al, 2015b), where different coupling problems are investigated. There – in some situations – fourth order is not achieved as well.

4.1.2 Non-Linear Loading Path

In a second example, order analysis is performed for cases with non-linear concentration loading (sinusoidal) as shown in Fig. 3(b). In this case, it can be noticed that the third and fourth order time-integration methods do not achieve the expected convergence orders, see Fig. 5. This is known as order reduction phenomenon, see (Alonso-Mallo, 2002; Alonso-Mallo and Cano, 2004). According to their proposal, the external loading functions are integrated as

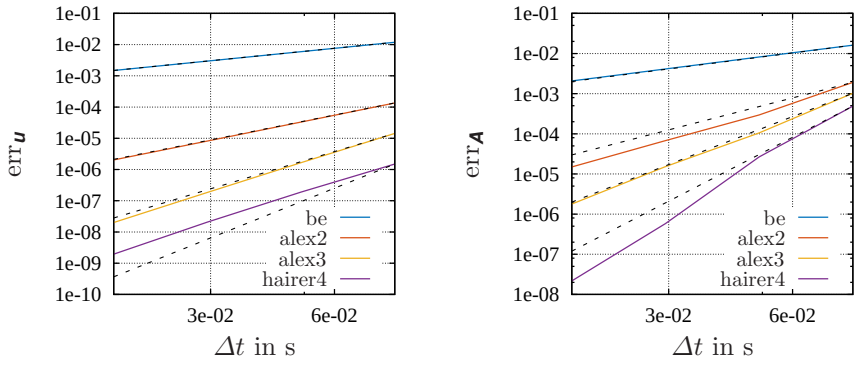

(a) Global error in displacement field (b) Global error in concentration field

Fig. 4: Convergence behavior for order analysis for linear loading path

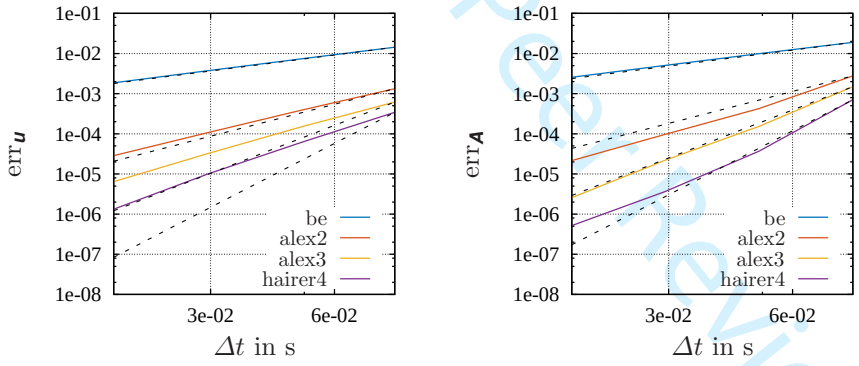

(a) Global error in displacement field (b) Global error in concentration field

Fig. 5: Convergence behavior for the order analysis of a sinusoidal loading path

well, see (Rothe et al, 2015b) and the literature cited therein. This circumvents with no essential effort the order reduction problem, see Fig. 6. Later on, this approach is followed.

4.2 Artery

In the second example, a three-dimensional model of an artery is chosen to demonstrate the principal applicability of the proposed coupling of diffusion

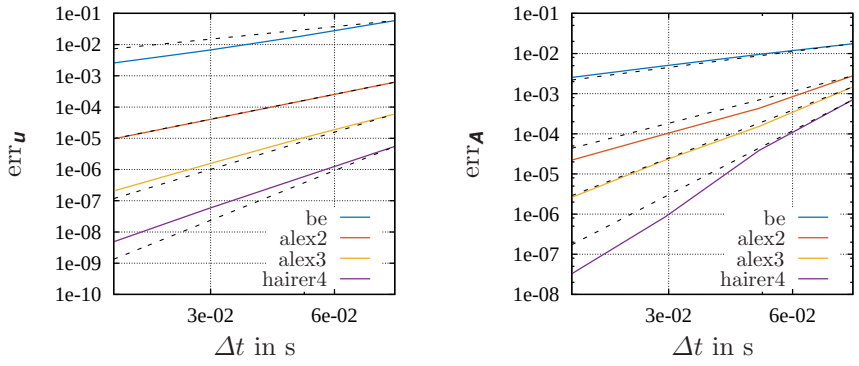

(a) Global error in displacement field (b) Global error in concentration field

Fig. 6: Convergence behavior for order analysis for non-linear loading path using (Alonso-Mallo, 2002; Alonso-Mallo and Cano, 2004) approach

with mechanical model by Yosibash and Priel (2012), see geometrical model in Fig. 7, The artery has approximately a length of 21 mm with a wall thickness

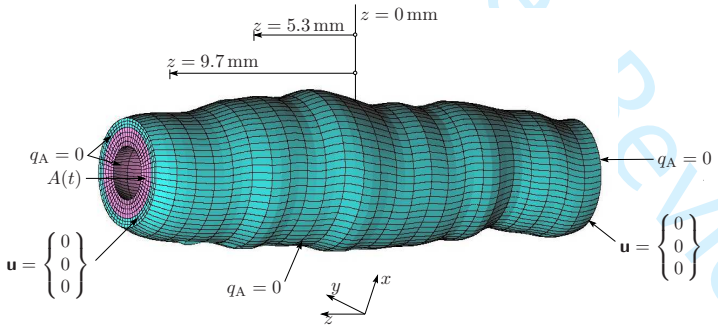

Fig. 7: Three-dimensional model of an artery

of 0.56 mm. The inner diameter of the artery is approximately 0.56 mm. The media is assumed to be twice the size of the adventitia and is approximately 0.37 mm . It is meshed using twenty-noded hexahedral elements leading to $n_{\text{el}} = 10500$ elements and resulting in a total number of $n_{\text{nodes}} = 47880$ nodes $((n_{\text{u}} = 136080,\ n_{\text{a}} = 43260))$.

The NE-concentration and the pressure are applied as boundary conditions on the inner side of the artery as in the case of real arteries. The pressure of the blood inside the artery is a periodic load taken from (Reitsamer and Kiel,

2002) for a rabbit. The pressure provided is required as input to the simulation and varies according to a periodic rhythm (here, we applied a Fourier series using the Curve Fitting Toolbox™ in Matlab® to obtain a continuous function varying between $50 - 80\text{mmHg}$, see Fig. 8(a)). Parallel to the pressure load,

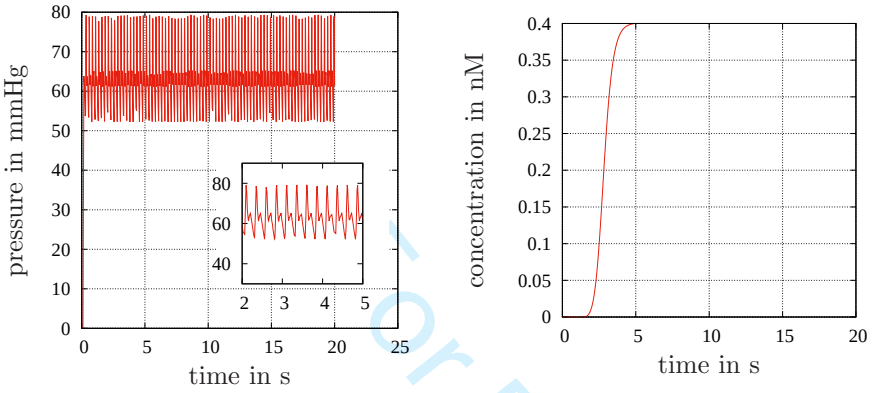

(a) Application of pressure on the inner side (b) Application of concentration on the inner side

Fig. 8: Mesh and boundary conditions applied on the inner side of the artery

the concentration increases from 0 to 0.4 nM at the inner side of the artery, see Fig. 8(b). The top and the bottom of the artery is fixed in all directions, which represent boundary conditions of an artery in an experiment. The material parameters are assumed to be same as that taken for the example in Section 4.1, see Tab. 1.

The results shown in Fig. 9 clearly demonstrate the activation of the artery under the influence of NE. The artery contracts and this change can be noticed in Fig. 9(b), where the change in inner diameter of 3 points at the inner side at three different locations along axial direction at $Z = 0\,\text{mm}$ (approximately half the length of the artery), $Z = 5.3\,\text{mm}$, and $Z = 9.7\,\text{mm}$ become negative after activation. The change in inner diameter at the same points on the inner surface of the artery with respect to the pressure before and after activation, can be seen in Fig. 9(a). The von Mises stress distribution inside the artery can be seen in Fig. 10 for two different times: Fig. 10(a) shows the undeformed configuration fo the modeled artery , whereas Fig. 10(b) visualizes the maximum pressure of a fully activated artery. It should be noted that the size of the deformation is in the order of magnitude of the experimental findings in (Wagner and Humphrey, 2011), see (Yosibash and Priel, 2012) as well.

Fig. 11(a) shows the step-size behavior of the entire process demonstrating the time-adaptivity. Using the step-size selection procedure in Section 3, the highly non-linear periodic loading process is computed. We draw on the

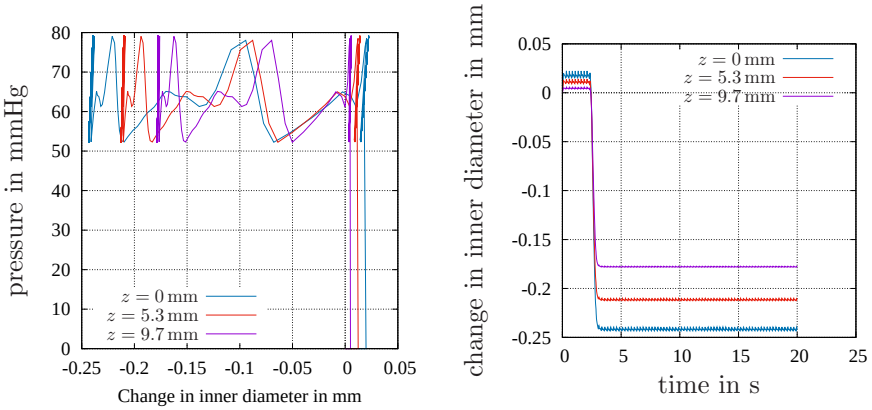

(a) Change in pressure with respect to change in inner diameter (b) Change in inner diameter with respect to time

Fig. 9: Results from the simulation of geometry reconstructed from a real artery

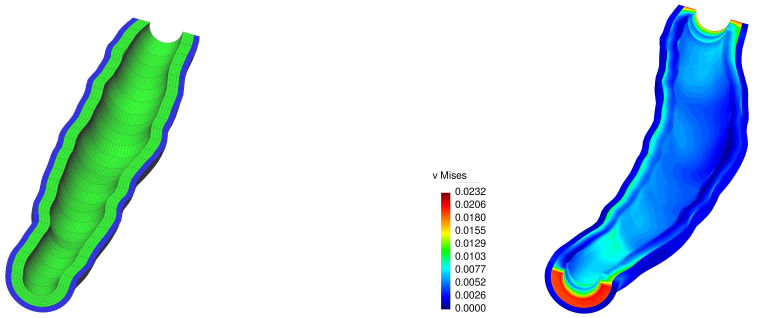

(a) Initial configuration and meshing of the artery

(b) Stress distribution at $t = 18.7\,\mathrm{sec}$; Maximum pressure, fully activated

Fig. 10: Undeformed configuration and von Mises stress distribution inside the artery (units in $\mathrm{N\,mm^{-2}}$)

method of (Ellsiepen, 1999), see (Ellsiepen and Hartmann, 2001) as well, which is a second-order accurate scheme (time-adaptive version) based on the second-order scheme of Alexander (1977). The step-size selection is mainly influenced by the highly non-linear loading process of the blood pressure. Furthermore, due to this non-linearity, a number of steps are rejected. The high number of rejections reduces the efficiency of the computation. In order to circumvent this problem, the new step-size selection procedure in Eq.(32) is chosen. This

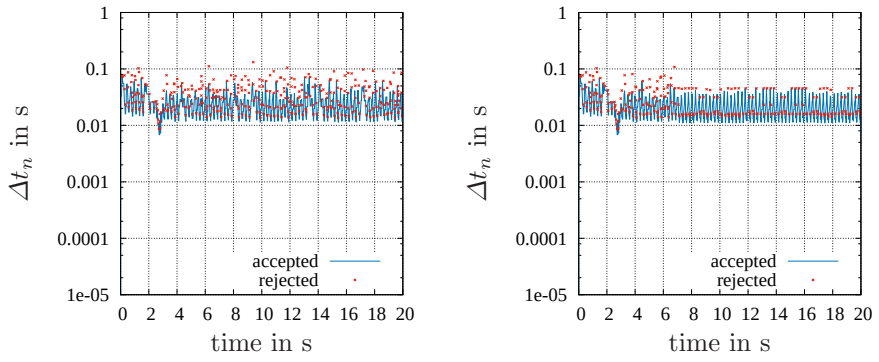

(a) Step-size selection procedure according to Eq.(31)

(b) Proposed step-size selection procedure of Eq.(32)

Fig. 11: Step-size behavior of the two schemes

procedure reduces the computational time by approximately 25%. The step-size behavior according to the new proposed scheme is shown in Fig. 11(b).

5 Conclusions

In this paper, we coupled - for the first time - the diffusion equation with the mechanical model proposed by Yosibash and Priel (2012) to reproduce the transient and non-local behavior of the activation of artery contractions. The method of vertical lines was applied to the diffusion-mechanical coupled problem leading – in the context of finite elements – to a large, coupled DAE-system. High-order time integration schemes were used to solve the resulting DAE-system in the time domain. The resulting non-linear system of equations were solved using Newton-Raphson method. Different high-order time integration schemes were investigated regarding their convergence order. In the case of linear loading of the concentration in the diffusion equations, it was observed that, except for the Hairer and Wanner method – first, second, and third-order methods (Backward-Euler method, Alexander's method of second and third order) achieve their respective orders. However, in the case of non-linear loading only second order was achieved. This problem, known as order reduction phenomenon, was circumvented by using the Alonso-Mallo (2002); Alonso-Mallo and Cano (2004) approach. Finally, a cyclic rhythm resembling the blood pressure cycle along with activation using NE was applied on a reconstructed pig artery to study the active response of the artery. Here, it becomes obvious that activation essentially changes the physical and geometrical behavior of an artery which is controlled by the diffused chemical in the

artery's wall. From the numerical point of view, we performed real pressure cycles leading to a considerable number of step-size rejections. These are minimized by a new step-size selection procedure considering the history of the periodic-like time steps as well. In our example, the proposed new scheme reduces the computational time by around 25%.

Acknowledgements The authors would like to thank Mr. Laszlo Kudela, Division of Computation in Engineering, Technische Universität München for providing the contour detection tool which was used to develop the 3D geometry of the artery. The financial support provided by the German-Israeli Foundation (GIF, grant no. I-89-202.17-2012) is also acknowledged by the authors.

Appendix A. The representation of the functional matrices

Applying spatial discretization of Eqns.(16) - (20) leads to the DAE-system (22) - (23) with the unknown nodal displacements $\boldsymbol{u} \in \mathbb{R}^{n_{\mathrm{u}}}$ and the unknown nodal concentrations $\boldsymbol{a} \in \mathbb{R}^{n_{\mathrm{a}}}$. Here,

$$\boldsymbol{g}(t,\boldsymbol{u},\boldsymbol{a}) = \sum_{e=1}^{n_{\mathrm{el}}} \boldsymbol{Z}_u^{e\,\mathrm{T}} \left[\sum_{k=1}^{n_{\mathrm{G}}^e} w_k \mathbf{B}_u^{e\,\mathrm{T}} \mathbf{F}_{23}^e \mathbf{h}^e(t, \mathbf{C}(\boldsymbol{u}), \boldsymbol{a}) \det \mathbf{j}^{\,e} \right] - \overline{\mathbf{p}}(t) = \boldsymbol{0}, \tag{34}$$

where $\boldsymbol{Z}_u^e$ is an assembling matrix containing zeros and ones (which is not programmed, representing the assembling procedure, but leading to a consistent matrix notation), w_k are the weighting factors of the Gaussian quadrature, $\mathbf{B}_u^e$ represents the strain-displacement matrix consisting of derivatives of the shape functions with respect to spatial coordinates, see, for example, (Bathe, 2002), $\mathbf{F}_{23}^e$ defines the push-forward operator, $\mathbf{h}^e$ symbolizes the elasticity relation defining the second Piola-Kirchhoff stresses, and $\det \mathbf{j}^{\,e}$ denotes the determinant of the Jacobian relative to the current configuration. For more detailed explanation, see (Hartmann, 2002, 2003).

$$\overline{\mathbf{p}}(t) = \int_{V_{\mathrm{R}}} \mathbf{N}_{\mathrm{u}}^{e\,\mathrm{T}} \rho \mathbf{k}^e \,\mathrm{d}V_{\mathrm{R}} + \int_{A_{\mathrm{R}}} \mathbf{N}_{\mathrm{u}}^{e\,\mathrm{T}} \mathbf{s}^e \,\mathrm{d}A_{\mathrm{R}} \tag{35}$$

is the vector containing volume distributed load and the traction force where $\mathbf{N}_{\mathrm{u}}^e$ is the matrix of shape function for the displacement and $\mathbf{s}^e$ are surface tractions.

$$\boldsymbol{C}(t,\boldsymbol{u},\boldsymbol{a}) = \sum_{e=1}^{n_{\mathrm{el}}} \boldsymbol{Z}_A^{e\,\mathrm{T}} \left[\sum_{k=1}^{n_{\mathrm{G}}^e} w_k \rho_{\mathrm{R}} \mathbf{N}_A^e \mathbf{N}_A^{e\,\mathrm{T}} \det \mathbf{J}^{\,e} \right] \boldsymbol{Z}_A^e, \quad \boldsymbol{C} \in \mathbb{R}^{n_{\mathrm{au}} \times n_{\mathrm{au}}} \tag{36}$$

represents a mass matrix like matrix. $\boldsymbol{Z}_A^e$ is the assembling matrix of the element contributions, $\mathbf{N}_A^e$ defines the vector of shape functions for the concentration approximation, and n_{au} denotes the number of unknown concentrations. The right-hand side of the differential part of the DAE-system (23) reads

$$\boldsymbol{r}_A(t,\boldsymbol{u},\boldsymbol{a}) = -\overline{\boldsymbol{C}}(t,\boldsymbol{u},\boldsymbol{a})\dot{\boldsymbol{a}} - \mathbf{p}_{\mathrm{D}}(t,\boldsymbol{u},\boldsymbol{a}) \tag{37}$$

where,

$$\overline{\boldsymbol{C}}(t,\boldsymbol{u},\boldsymbol{a}) = \sum_{e=1}^{n_{\mathrm{el}}} \boldsymbol{Z}_A^{e\,\mathrm{T}} \left[\sum_{k=1}^{n_{\mathrm{G}}^e} w_k \rho_{\mathrm{R}} \mathbf{N}_A^e \mathbf{N}_A^{e\,\mathrm{T}} \det \mathbf{J}^{\,e} \right] \overline{\boldsymbol{Z}}_A^e, \quad \overline{\boldsymbol{C}} \in \mathbb{R}^{n_{\mathrm{au}} \times n_{\mathrm{ap}}}, \tag{38}$$

$\overline{\boldsymbol{Z}}_A^e$ is a matrix containing zeros and ones to represent the known concentrations and n_{ap} represents the number of prescribed concentrations. The second term in Eq.(37) reads

$$\mathbf{p}_{\mathrm{D}}(t,\boldsymbol{u},\boldsymbol{a}) = \boldsymbol{C}_{\mathrm{D}}(t,\boldsymbol{u},\boldsymbol{a})\boldsymbol{a}(t) + \overline{\boldsymbol{C}}_{\mathrm{D}}(t,\boldsymbol{u},\boldsymbol{a})\overline{\boldsymbol{a}}(t) \tag{39}$$

with

$$\boldsymbol{C}_{\mathrm{D}}(t,\boldsymbol{u},\boldsymbol{a}) = \sum_{e=1}^{n_{\mathrm{el}}} \boldsymbol{Z}_A^{e\,\mathrm{T}} \left[\sum_{k=1}^{n_{\mathrm{G}}^e} w_k D\, \mathbf{B}_A^e\, \mathbf{B}_A^{e\,\mathrm{T}} \det \mathbf{j}^{\,e} \right] \boldsymbol{Z}_A^e, \quad \boldsymbol{C}_{\mathrm{D}} \in \mathbb{R}^{n_{\mathrm{au}} \times n_{\mathrm{au}}}, \tag{40}$$

and

$$\overline{\boldsymbol{C}}_{\mathrm{D}}(t,\boldsymbol{u},\boldsymbol{a}) = \sum_{e=1}^{n_{\mathrm{el}}} \boldsymbol{Z}_A^{e\,\mathrm{T}} \left[\sum_{k=1}^{n_{\mathrm{G}}^e} w_k D\, \mathbf{B}_A^e\, \mathbf{B}_A^{e\,\mathrm{T}} \det \mathbf{j}^{\,e} \right] \overline{\boldsymbol{Z}}_A^e, \quad \overline{\boldsymbol{C}}_{\mathrm{D}} \in \mathbb{R}^{n_{\mathrm{au}} \times n_{\mathrm{ap}}}, \tag{41}$$

$\mathbf{B}_A^e \in \mathbb{R}^{n_A^e}$ is a vector similar to the strain-displacement matrix consisting of the derivatives of shape functions of the concentration with respect to spatial coordinates. n_A^e define the element degrees of freedom of the concentration, and D the diffusion coefficient. The coupling of Eq.(23) to the deformation (displacements) is given by $\mathbf{FJ} = \mathbf{j}$. Thus, the DAE-system (22) - (23) represents a two-way coupled (fully coupled) problem.

Appendix B. The parameters of the applied DIRK-methods

Tab. 2 shows all the factors of the DIRK-methods used for the examples studied in Sec. 4.

Table 2: Butcher-Tableaus of the different DIRK methods

(a) Backward Euler (be) $(s = 1, p = 1)$

1	1
	1

(b) Alexander/Ellsiepen (alex2) $(s = 2, p = 2, \hat{p} = 1)$

α	α	
1	$1-\alpha$	α
	$1-\alpha$	α
	$1-\hat{\alpha}$	$\hat{\alpha}$

$\alpha = 1 - \frac{1}{2}\sqrt{2}, \qquad \hat{\alpha} = 2 - \frac{5}{4}\sqrt{2}$

(c) Alexander/Cash (alex3) $(s = 3, p = 3, \hat{p} = 2)$

γ	γ		
δ	$\tau-\gamma$	γ	
1	α	β	γ
	α	β	γ
	$\hat{\alpha}$	$\hat{\beta}$	0

$\gamma = 0.4358665215084580$
$\tau - \gamma = 0.2820667392457705$
$\alpha = 1.2084966491760101$
$\beta = -0.6443631706844691$
$\delta = 0.7179332607542295$
$\hat{\alpha} = 0.7726301276675511$
$\hat{\beta} = 0.2273698723324489$

(d) Hairer & Wanner (hairer4) $(s = 5, p = 4, \hat{p} = 3)$

$\frac{1}{4}$	$\frac{1}{4}$				
$\frac{3}{4}$	$\frac{1}{2}$	$\frac{1}{4}$			
$\frac{11}{20}$	$\frac{17}{50}$	$-\frac{1}{25}$	$\frac{1}{4}$		
$\frac{1}{2}$	$\frac{371}{1360}$	$-\frac{137}{2720}$	$\frac{15}{544}$	$\frac{1}{4}$	
1	$\frac{25}{24}$	$-\frac{49}{48}$	$\frac{125}{16}$	$-\frac{85}{12}$	$\frac{1}{4}$
	$\frac{25}{24}$	$-\frac{49}{48}$	$\frac{125}{16}$	$-\frac{85}{12}$	$\frac{1}{4}$
	$\frac{59}{48}$	$-\frac{17}{96}$	$\frac{225}{32}$	$-\frac{85}{12}$	0

References

Alexander R (1977) Diagonally implicit Runge-Kutta methods for stiff O.D.E.'s. SIAM Journal on Numerical Analysis 14:1006–1021

Alonso-Mallo I (2002) Runge-Kutta methods without order reduction for linear initial boundary value problems. Numerische Mathematik 91(4):577–603

Alonso-Mallo I, Cano B (2004) Avoiding order reduction of Runge-Kutta discretizations for linear time-dependent parabolic problems. BIT Numerical Mathematics 44:1–20

Aoki H, Nishimura J, Kobayashi S, Kanaide H (1994) Relationship between cytosolic calcium concentration and force in the papaverine-induced relaxation of medial strips of pig coronary artery. British Journal of Pharmacology 111:489–496

Ascher UM, Petzold LR (1998) Computer methods for ordinary differential equations and differential-algebraic equations. SIAM Society for Industrial and Applied Mathematics, Philadelphia

Barany M (1996) Biochemistry of Smooth Muscle Contraction. Elsevier Science

Bathe KJ (2002) Finite - Elemente - Methoden, 1st edn. Springer, Berlin

Böl M, Schmitz A, Nowak G, Siebert T (2012) A three-dimensional chemo-mechanical continuum model for smooth muscle contraction. Journal of the Mechanical Behavior of Biomedical Materials 13:215–229

Cash JR (1979) Diagonally implicit Runge-Kutta formulae with error estimates. Journal of the Institute of Mathematics and its Applications 24:293–301

Chamiot-Clerc P, Copie X, Renaud JF, Safar M, Girerd X (1998) Comparative reactivity and mechanical properties of human isolated internal mammary and radial arteries. Cardiovascular Research 37:811–819

Chen H, Luo T, Zhao X, Lu X, Huo Y, Kassab GS (2013a) Microstructural constitutive model of active coronary media. Biomaterials 34:7575–7583

Chen X, Summers RM, Yao J (2013b) Kidney tumor growth prediction by coupling reaction diffusion and biomechanical model. IEEE Transactions on Biomedical Engineering 60(1):169–173

Cox RH (1978a) Comparison of carotid artery mechanics in the rat, rabbit and dog. The American Journal of Physiology 234(3):H280–H288

Cox RH (1978b) Regional variation of series elasticity in canine arterial smooth muscles. The American Journal of Physiology 234(5):H542–H551

De La Lande I, Jellett L, Lazner MA, Parker D, Waterson J (1974) Histochemical analysis of the diffusion of noradrenaline across the artery wall. Australian Journal of Experimental Biology and Medical Science 52(1):193–200

Delfino A, Stergiopulos N, Moore JE, Meister JJ (1997) Residual strain effects on the stress field in a thick wall finite element model of the human carotid bifurcation. Journal of Biomechanics 30:777–786

Diebels S, Ellsiepen P, Ehlers W (1999) Error-controlled Runge-Kutta time integration of a viscoplastic hybrid two-phase model. Technische Mechanik 19:19–27

Eckert S, Baaser H, Gross D, Scherf O (2004) A BDF2 integration method with stepsize control for elastoplasticity. Computational Mechanics 34(5):377–386

Ellsiepen P (1999) Zeit- und ortsadaptive Verfahren angewandt auf Mehrphasenprobleme poröser Medien. Doctoral thesis, Institute of Mechanics II, University of Stuttgart, report No. II-3

Ellsiepen P, Hartmann S (2001) Remarks on the interpretation of current non-linear finite-element-analyses as differential-algebraic equations. International Journal for Numerical Methods in Engineering 51:679–707

Erbts P, Düster A (2012) Accelerated staggered coupling schemes for problems of thermoelasticity at finite strains. Computers & Mathematics with Applications 64(8):2408–2430

Erbts P, Hartmann S, Düster A (2015) A partitioned solution approach for electro-thermomechanical problems. Archive of Applied Mechanics 85:1075–1101

Fritzen P (1997) Numerische Behandlung nichtlinearer Probleme der Elastizitäts- und Plastizitätstheorie. Doctoral thesis, Department of Mathematics, University of Darmstadt

Fung YC, Fronek K, Patitucci P (1979) Pseudoelasticity of arteries and of its mathematical expression. American Physiological Society 237:H620–H631

Gestrelius S, Borgstrom P (1986) A dynamic model of smooth muscle contraction. Biophysical Journal 50:157–169

Gilbert RR, Hartmann S, Kudela L, Rank E, Sahar G, Yosibash Z, Yossef O (2016) Parameter identification of the passive response in arteries. Technical Report Series Fac3-16-01, Faculty of Mathematics/Computer Science and Mechanical Engineering, Clausthal University of Technology (Germany)

Gleim T, Schröder B, Kuhl D (2015) Nonlinear thermo-electromagnetic analysis of inductive heating processes. Archive of Applied Mechanics 85(8):1055–1073

Grafenhorst M, Rang J, Hartmann S (2017) Time-adaptive finite element simulations of dynamical problems for temperature-dependent materials. Journal of Mechanics of Materials and Structures 12(1):57–91

Grover A, Daniels E (2012) Calcium and Contractility: Smooth Muscle. Contemporary Biomedicine, Humana Press

Gustafsson K (1994) Control-Theoretic Techniques for Stepsize Selection in Implicit Runge-Kutta Methods. Transactions on Mathematical Software 20(4):496–517, DOI 10.1145/198429.198437

Gustafsson K, Lundh M, Söderlind G (1988) A PI Stepsize Control for the Numerical Solution of Ordinary Differential Equations. BIT Numerical Mathematics 28(2):270–287, DOI 10.1007/BF01934091

Hai CM, Murphy RA (1988) Cross-bridge phosphorylation and regulation of latch state in smooth muscle. The American Journal of Physiology 254:C99–106

Hairer E, Wanner G (1996) Solving Ordinary Differential Equations II, 2nd edn. Springer, Berlin

Hairer E, Lubich C, Roche M (1989) The numerical solution of differential-algebraic systems by Runge-Kutta methods. Springer-Verlag, Berlin

Hairer E, Norsett SP, Wanner G (1993) Solving Ordinary Differential Equations I, 2nd edn. Springer, Berlin

Hamill RW, Shapiro RE, Vizzard M (1996) Peripheral autonomic nervous system. Primer on the autonomic nervous system pp 12–25

Hamkar AW (2013) Eine iterationsfreie Finite-Elemente Methode im Rahmen der finiten Thermoviskoelastizität. Phd-thesis, report no. 1/2013, Institute of Applied Mechanics, Clausthal University of Technology, Clausthal-Zellerfeld

Hamkar AW, Hartmann S (2012) Theoretical and numerical aspects in weak-compressible finite strain thermo-elasticity. Journal of Theoretical and Applied Mechanics 50:3–22

Hamkar AW, Hartmann S, Rang J (2012) A stiffly accurate Rosenbrock-type method of order 2 applied to FE-analyses in finite strain viscoelasticity. Applied Numerical Mathematics 62(12):1837 – 1848

Hartmann S (2002) Computation in finite strain viscoelasticity: finite elements based on the interpretation as differential-algebraic equations. Computer Methods in Applied Mechanics and Engineering 191(13-14):1439–1470

Hartmann S (2003) Finite-Elemente Berechnung inelastischer Kontinua. Interpretation als Algebro-Differentialgleichungssysteme. Habilitation, University of Kassel, Institute of Mechanics, report No. 1/2003

Hartmann S (2005) A remark on the application of the Newton-Raphson method in non-linear finite element analysis. Computational Mechanics 36(2):100–116

Hartmann S, Neff P (2003) Polyconvexity of generalized polynomial-type hyperelastic strain energy functions for near-incompressibility. International Journal of Solids and Structures 40:2767–2791

Hartmann S, Rothe S (2013) A rigorous application of the method of vertical lines to coupled systems in finite element analysis. In: Ansorge R, Bijl H, Meister A, Sonar T (eds) Recent Developments in the Numerics of Nonlinear Hyperbolic Conservation Laws, Notes on Numerical Fluid Mechanics and Multidisciplinary Design, vol 120, Springer Berlin / Heidelberg, pp 161–175

Hartmann S, Duintjer Tebbens J, Quint KJ, Meister A (2009a) Iterative solvers within sequences of large linear systems in non-linear structural mechanics. ZAMM Journal of Applied Mathematics and Mechanics 89(9):711–728

Hartmann S, Kuhl D, Quint KJ (2009b) Time-adaptive computation of thermoviscoplastic structures. In: Steinhoff K, Maier HJ, Biermann D (eds) Functionally graded materials

in industrial mass production, Verlag Wissenschaftliche Scripten, Auerbach (Germany), chap 3.1, pp 269 – 282
Hermsmeyer K (1983) Excitation of vascular muscle by norepinephrine. Annals of Biomedical Engineering 11(6):567–577
Hollander Y, Durban D, Lu X, Kassab GS, Lanir Y (2011) Constitutive modeling of coronary arterial media–comparison of three model classes. Journal of Biomechanical Engineering 133:061,008–061,020
Holzapfel GA, Gasser TC, Ogden RW (2000) A new constitutive framework for arterial wall mechanics and a comparative study of material models. Journal of Elasticity 61:1–48
Holzapfel GA, Gasser TC, Stadler M (2002) A structural model for the viscoelastic behavior of arterial walls: Continuum formulation and finite element analysis. European Journal of Mechanics - A/Solids 21:441–463
Humphrey J (2002) Cardiovascular Solid Mechanics: Cells, Tissues, and Organs. Springer
Huo Y, Cheng Y, Zhao X, Lu X, Kassab GS (2012) Biaxial vasoactivity of porcine coronary artery. American Journal of Physiology: Heart and Circulatory Physiology 302:H2058–H2063
Huxley H (1953) Electron microscope studies of the organisation of the filaments in striated muscle. Biochimica et Biophysica Acta 12(1):387 – 394
Itskov M, Ehret AE (2009) A universal model for the elastic, inelastic and active behaviour of soft biological tissues. GAMM-Mitteilungen 32:221–236
Klabunde R (2005) Cardiovascular Physiology Concepts. Lippincott Williams & Wilkins
Kuhl D, Meschke G (2003) Computational modeling of transport mechanisms in reactive porous media-application to calcium leaching of concrete. Computational Modelling of Concrete Structures pp 473–482
Kuhl D, Meschke G (2004) Robust time integration schemes for durability analyses. In: Proceedings of the Sixth World Congress on Computational Mechanics (WCCM V)
Kuhl D, Bangert F, Meschke G (2004a) Coupled chemo-mechanical deterioration of cementitious materials. part i: Modeling. International Journal of Solids and Structures 41(1):15 – 40
Kuhl D, Bangert F, Meschke G (2004b) Coupled chemo-mechanical deterioration of cementitious materials part ii: Numerical methods and simulations. International Journal of Solids and Structures 41(1):41 – 67
Lefèvre J, Mangin JF (2010) A reaction-diffusion model of the human brain development. In: 2010 IEEE International Symposium on Biomedical Imaging: From Nano to Macro, pp 77–80
Mecham R, Schwartz S (1995) The Vascular Smooth Muscle Cell: Molecular and Biological Responses to the Extracellular Matrix. Biology of Extracellular Matrix, Elsevier Science
Menze BH, Stretton E, Konukoglu E, Ayache N (2011) Image-based modeling of tumor growth in patients with glioma. In: Garbe CS, Rannacher R, Platt U, Wagner T (eds) Optimal control in image processing, Springer, Heidelberg/Germany
Murtada SI, Humphrey JD, Holzapfel GA (2017) Multiscale and multiaxial mechanics of vascular smooth muscle. Biophysical Journal 113(3):714–727
Murtada SIC, Holzapfel GA (2014) Investigating the role of smooth muscle cells in large elastic arteries: A finite element analysis. Journal of Theoretical Biology 358:1 – 10
Murtada SIC, Kroon M, Holzapfel GA (2010) A calcium-driven mechanochemical model for prediction of force generation in smooth muscle. Biomechanics and Modeling in Mechanobiology 9:749–762
Murtada SIC, Arner A, Holzapfel GA (2012) Experiments and mechanochemical modeling of smooth muscle contraction: Significance of filament overlap. Journal of Theoretical Biology 297:176 – 186
Netz T (2013) High-order space and time discretization scheme applied to problems of finite thermo-viscoelasticity. Phd-thesis, report no. 3/2013, Institute of Applied Mechanics, Clausthal University of Technology, Clausthal-Zellerfeld
Netz T, Hartmann S (2015) A monolithic finite element approach using high-order schemes in time and space applied to finite strain thermo-viscoelasticity. Computers and Mathematics with Applications 70:1457–1480
Netz T, Hamkar AW, Hartmann S (2013) High-order quasi-static finite element computations in space and time with application to finite strain viscoelasticity. Computers and

Mathematics with Applications 66:441 – 459
Nolan DR, Gower AL, Destrade M, Ogden RW, McGarry JP (2014) A robust anisotropic hyperelastic formulation for the modelling of soft tissue. Journal of the Mechanical Behavior of Biomedical Materials 39:48–60
Pandolfi A, Gizzi A, Vasta M (2016) Coupled electro-mechanical models of fiber-distributed active tissues. Journal of Biomechanics 49(12):2436 – 2444, cardiovascular Biomechanics in Health and Disease
Piatnitski A, Ptashnyk M (2017) Homogenization of biomechanical models for plant tissues. Multiscale Modeling & Simulation 15(1):339–387
Ptashnyk M, Seguin B (2016) Homogenization of a system of elastic and reaction-diffusion equations modelling plant cell wall biomechanics. Esaim: Mathematical Modelling and Numerical Analysis 50(2):593–631
Quint KJ (2012) Thermomechanically coupled processes for functionally graded materials: experiments, modelling, and finite element analysis using high-order DIRK-methods. Phd-thesis, report no. 2/2012, Institute of Applied Mechanics, Clausthal University of Technology, Clausthal-Zellerfeld
Rachev A, Hayashi K (1999) Theoretical study of the effects of vascular smooth muscle contraction on strain and stress distributions in arteries. Annals of Biomedical Engineering 27:459–468
Reitsamer HA, Kiel JW (2002) A rabbit model to study orbital venous pressure, intraocular pressure, and ocular hemodynamics simultaneously. Investigative Ophthalmology & Visual Science 43 12:3728–3734
Rhodin JAG (2011) Architecture of the vessel wall. Comprehensive Physiology pp 1–31
Rothe S (2015) Electro-thermo-mechanical modeling of field assisted sintering technology: Experiments, constitutive modeling and finite element analysis. Phd-thesis, report no. 1/2015, Institute of Applied Mechanics, Clausthal University of Technology, Clausthal-Zellerfeld
Rothe S, Hamkar AW, Quint KJ, Hartmann S (2012) Comparison of diagonal-implicit, linear-implicit and half-explicit Runge-Kutta methods in non-linear finite element analyses. Archive of Applied Mechanics 82(8):1057 – 1074
Rothe S, Erbts P, Düster A, Hartmann S (2015a) Monolithic and partitioned coupling schemes for thermo-viscoplasticity. Computer Methods in Applied Mechanics and Engineering 293:375 – 410
Rothe S, Schmidt JH, Hartmann S (2015b) Analytical and numerical treatment of electro-thermo-mechanical coupling. Archive of Applied Mechanics 85:1245–1264
Schmitz A, Böl M (2011) On a phenomenological model for active smooth muscle contraction. Journal of Biomechanics 44:2090–2095
Sepahi O, Radtke L, Debus S, Düster A (2017) Anisotropic hierarchic solid finite elements for the simulation of passive-active arterial wall models. Computers & Mathematics with Applications 74(12):3058 – 3079
Sharifimajd B, Stålhand J (2014) A continuum model for excitationcontraction of smooth muscle under finite deformations. Journal of Theoretical Biology 355:1 – 9
Stålhand J, Klarbring A, Holzapfel GA (2008) Smooth muscle contraction: mechanochemical formulation for homogeneous finite strains. Progress in Biophysics and Molecular Biology 96(1-3):465–481
Stålhand J, Klarbring A, Holzapfel GA (2011) A mechanochemical 3D continuum model for smooth muscle contraction under finite strains. Journal of Theoretical Biology 268:120–130
Stålhand J, McMeeking RM, Holzapfel GA (2016) On the thermodynamics of smooth muscle contraction. Journal of the Mechanics and Physics of Solids 94:490 – 503
Strehmel K, Weiner R (1995) Numerik gewöhnlicher Differentialgleichungen. Teubner, Stuttgart
Wagner HP, Humphrey JD (2011) Differential passive and active biaxial mechanical behaviors of muscular and elastic arteries: basilar versus common carotid. Journal of Biomechanical Engineering 133(5):051,009
Wendt G, Erbts P, Düster A (2015) Partitioned coupling strategies for multi-physically coupled radiative heat transfer problems. Journal of Computational Physics 300:327–351

Wittekindt J (1991) Die numerische Lösung von Anfangs-Randwertproblemen zur Beschreibung inelastischen Werkstoffverhaltens. Doctoral thesis, Department of Mathematics, University of Darmstadt

Wong KC, Summers RM, Kebebew E, Yao J (2015) Tumor growth prediction with reaction-diffusion and hyperelastic biomechanical model by physiological data fusion. Medical Image Analysis 25(1):72 – 85

Yosibash Z, Priel E (2012) Artery active mechanical response: High order finite element implementation and investigation. Computer Methods in Applied Mechanics and Engineering 237-240:51–66

Zhou B, Rachev A, Shazly T (2015) The biaxial active mechanical properties of the porcine primary renal artery. Journal of the mechanical behavior of biomedical materials 48:28–37

Zulliger MA, Fridez P, Hayashi K, Stergiopulos N (2004a) A strain energy function for arteries accounting for wall composition and structure. Journal of Biomechanics 37:989–1000

Zulliger MA, Rachev A, Stergiopulos N (2004b) A constitutive formulation of arterial mechanics including vascular smooth muscle tone. American Journal of Physiology: Heart and Circulatory Physiology 287:H1335–H1343